A Meteorological Distribution System for High-Resolution Terrestrial Modeling (MicroMet)

GLEN E. LISTON

Department of Atmospheric Science, Colorado State University, Fort Collins, Colorado

KELLY ELDER

Rocky Mountain Research Station, USDA Forest Service, Fort Collins, Colorado

(Manuscript received 12 November 2004, in final form 12 September 2005)

ABSTRACT

An intermediate-complexity, quasi–physically based, meteorological model (MicroMet) has been developed to produce high-resolution (e.g., 30-m to 1-km horizontal grid increment) atmospheric forcings required to run spatially distributed terrestrial models over a wide variety of landscapes. The following eight variables, required to run most terrestrial models, are distributed: air temperature, relative humidity, wind speed, wind direction, incoming solar radiation, incoming longwave radiation, surface pressure, and precipitation. To produce these distributions, MicroMet assumes that at least one value of each of the following meteorological variables are available for each time step, somewhere within, or near, the simulation domain: air temperature, relative humidity, wind speed, wind direction, and precipitation. These variables are collected at most meteorological stations. For the incoming solar and longwave radiation, and surface pressure, either MicroMet can use its submodels to generate these fields, or it can create the distributions from observations as part of a data assimilation procedure. MicroMet includes a preprocessor component that analyzes meteorological data, then identifies and corrects potential deficiencies. Since providing temporally and spatially continuous atmospheric forcing data for terrestrial models is a core objective of MicroMet, the preprocessor also fills in any missing data segments with realistic values. Data filling is achieved by employing a variety of procedures, including an autoregressive integrated moving average calculation for diurnally varying variables (e.g., air temperature). To create the distributed atmospheric fields, spatial interpolations are performed using the Barnes objective analysis scheme, and subsequent corrections are made to the interpolated fields using known temperature–elevation, wind–topography, humidity–cloudiness, and radiation–cloud–topography relationships.

1. Introduction

For decades, earth-system scientists have been developing physically based mathematical models describing interactions between the atmosphere and terrestrial surface. These models represent important climate system components and have improved our understanding of climate-related processes and feedbacks. The latest generations of distributed terrestrial models are being designed for high spatial resolutions (e.g., 30-m to 1-km horizontal grid increments) and require scale-appropriate atmospheric forcings. For example, models require spatially relevant driving data to simulate river discharge and floods (e.g., Jasper et al. 2002; Westrick et al. 2002), ecosystem processes (e.g., Le Dizès et al. 2003; Vourlitis et al. 2003), snow distributions (e.g., Liston and Sturm 2002; Winstral et al. 2002), soil temperatures and active layers (e.g., Shiklomanov and Nelson 2002; Taras et al. 2002), and water cycles using soil–vegetation–atmosphere interaction models (e.g., Ludwig and Mauser 2000; Whitaker et al. 2003).

In addition to providing high-resolution information on terrestrial features and fluxes, high-resolution models can be used to develop parameterizations of subgrid features found within low-resolution atmospheric and terrestrial models (e.g., Randall et al. 2003; Liston 2004). This is accomplished by running the models as explicit subgrid-process-resolving models, and using the resulting information to understand the interrelationships among the relatively small and large scales.

Corresponding author address: Dr. Glen E. Liston, Cooperative Institute for Research in the Atmosphere, Colorado State University, Fort Collins, CO 80523-1375.
E-mail: liston@cira.colostate.edu

Many spatially distributed terrestrial models require atmospheric forcings on surface grids having higher spatial resolution than the available meteorological data. In the absence of appropriate gridded atmospheric data, these models are forced to employ point data to represent meteorological conditions across their simulation domains. In our search for methods to generate the required distributed atmospheric forcing, we find that it is computationally prohibitive to run fully dynamic, regional atmospheric models (e.g., Liston et al. 1999; Liston and Pielke 2001) over full annual cycles at subkilometer grid increments, and that simple interpolation schemes may not account for naturally occurring meteorological gradients. Thus, computationally efficient and physically realistic methods must be developed to take available meteorological datasets (e.g., meteorological station observations, and/or regional atmospheric model or analyses datasets on, say, 10-km grids) and generate required high-resolution atmospheric-forcing distributions.

This paper describes MicroMet, an intermediate-complexity meteorological model designed to produce high-resolution (e.g., 30-m to 1-km horizontal grid increments) meteorological data distributions required to run spatially distributed terrestrial models over a wide variety of landscapes. The following eight variables are distributed: air temperature, relative humidity, wind speed, wind direction, incoming solar radiation, incoming longwave radiation, surface pressure, and precipitation. Preliminary, largely undocumented and incomplete versions of MicroMet have been used to successfully distribute both observed and modeled meteorological variables over complex terrain in Colorado, Wyoming, Idaho, Arctic Alaska, Svalbard, central Norway, Greenland, and Antarctica as part of a wide variety of terrestrial modeling studies (e.g., Liston and Sturm 1998, 2002; Greene et al. 1999; Liston et al. 1999, 2000, 2002; Prasad et al. 2001; Hiemstra et al. 2002; 2005, manuscript submitted to *Wea. Forecasting*; 2006; Taras et al. 2002; Hasholt et al. 2003; Bruland et al. 2004; Liston and Elder 2005, manuscript submitted to *J. Hydrometeor.*; Liston and Winther 2005).

2. MicroMet data preprocessor

MicroMet includes a three-step preprocessor that analyzes meteorological station data (or model grid-point data) and identifies and/or corrects deficiencies. While MicroMet can be run using any time step from 1 min to 1 day, the following preprocessor discussion assumes the raw station data are provided on an hourly time increment. In addition, as part of the preprocessing steps, each meteorological variable for all stations must be converted to a common height (e.g., 2.0 or 10.0 m) using appropriate transfer functions, such as the logarithmic wind profile equation for wind speed. This decision then defines the height(s) of the MicroMet-simulated meteorological distributions.

First, the preprocessor fills the variables for missing dates/times with an "undefined" value (e.g., −9999.0). This filling is done before any data quality assurance/quality control (QA/QC) tests because it would be useless to compare two adjacent values that are separated by missing data.

Second, the preprocessor performs a series of QA/QC data tests following Meek and Hatfield (1994). The tests consider three conditions/cases: case 1 checks for values outside acceptable ranges, high/low range limits (LIM); case 2 seeks consecutive values that exceed acceptable increments, rate-of-change limits (ROC); case 3 finds constant consecutive values with no-observed-change within time limits (4 h) (NOC). For example, unchanging wind directions or repeating zero wind speeds might indicate an iced or otherwise defective instrument.

Third, the preprocessor fills in missing time series data with calculated values. The implemented data-fill procedures assume that as long as the data of interest are within a given synoptic cycle, persistence is a reasonable approximation. In general, at a given point, the weather today is frequently similar to what it was yesterday and what it will be tomorrow (Jolliffe and Stephenson 2003). This assumption is dependent on time of year and geographic location; it becomes less tenable as the length of missing data becomes larger, as we discuss later.

MicroMet fills missing data segments in a variety of ways. Air temperature, relative humidity, wind speed and direction, and precipitation, are all assumed to have diurnal cycles, and the data-fill procedure is different for each of the following three conditions (Fig. 1): Condition 1 contains a single missing data value (i.e., one missing hour) where the datum for that hour is defined to be the average of the values an hour before and after the missing hour (Fig. 1a). Condition 2 has missing data segments ranging from 2 to 24 h and missing values are determined as an average of the values from 24 h before and after each of the missing hours in that period (Fig. 1b). This solution has the attractive feature of preserving the variables' diurnal cycle. Last, condition 3 includes missing data segments larger than 24 h (Fig. 1c). For this condition, the time series prediction is made using an autoregressive integrated moving average (ARIMA) model (Box and Jenkins 1976). The implemented formulation closely follows the ideas

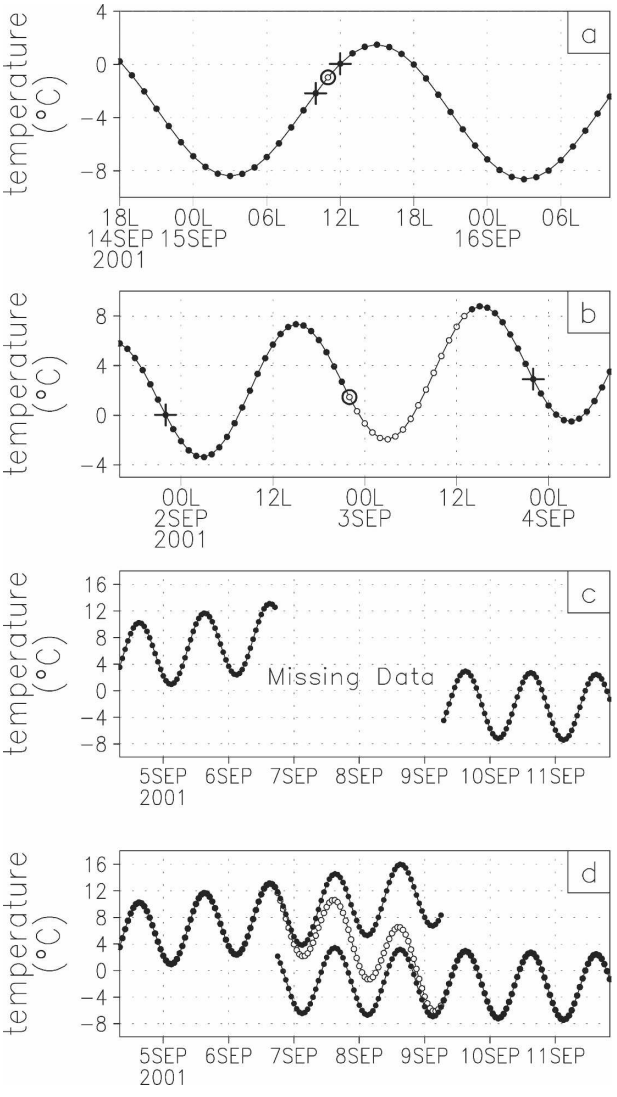

FIG. 1. Example MicroMet preprocessor data-filling procedure for air temperature. (a) Condition 1: 1 h of missing data (data at the crosses are averaged to fill the missing hour). (b) Condition 2: greater than one, but less than 25 h of missing data (data at the crosses, located 24 h before and after each missing hour, are averaged to fill each missing hour). (c) Condition 3: illustrating more than 24 h of missing data, where the missing time period is filled (d) by extrapolating forward and backward (in the missing data section), using an ARIMA model, and linearly weighting the two results (shown by the open markers).

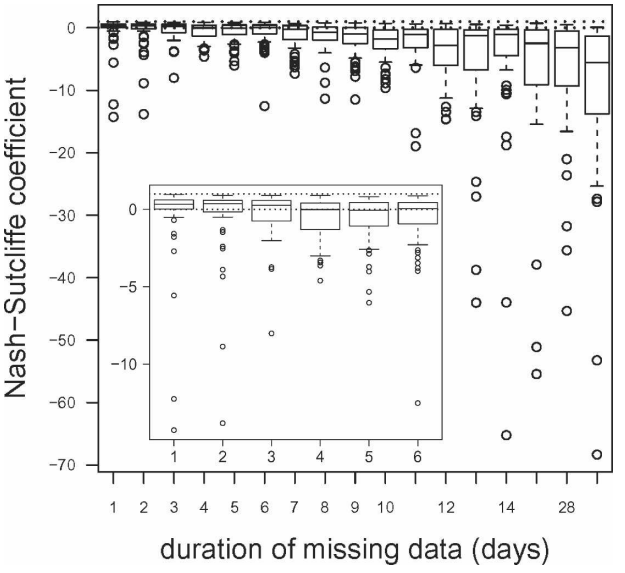

FIG. 2. Results of goodness-of-fit tests for missing data periods using NSC for different missing data durations. The lines in the middle of the boxes show the median NSC values for each data-filling period. The upper and lower bounds of the boxes show the inner quartile ranges. The whiskers show the ranges of the highest values that lie within twice the inner quartile ranges. Open circles show data values that lie outside twice the inner quartile ranges. The top horizontal dotted line (NSC = 1) represents a perfect fit. Values falling below the lower dotted line (NSC = 0) indicate major deviations between modeled and observed data. The inset shows details of the first 6 days.

presented in Walton (1996). In the MicroMet preprocessor, we use an ARIMA model to forecast into the missing segment using data preceding the missing segment and backcast into the missing segment using data following the missing segment (both using data spans equal in length to the missing-data span). The two results are then linearly interpolated across the data gap (Fig. 1d).

The preprocessor was tested to evaluate the data-filling procedure. For this task, the National Aeronautics and Space Administration (NASA) Cold Land Processes Field Experiment's (CLPX; Cline et al. 2005, manuscript submitted to *J. Hydrometeor.*; Goodbody et al. 2005, manuscript submitted to *J. Hydrometeor.*) Walton Creek meteorological station air temperature record for 23 September 2002 through 27 September 2003 was selected because it contained no missing data. This tower is located in a treeless meadow in the Park Range, Colorado, at 40°24.0′N, 106°38.7′W, and 2950-m elevation. To create missing data for the Walton Creek data, a random sampling scheme was used to define 50 different initial start times (date and hour of day). For each start time, data for 1 through 14, 21, 28, and 35 days were removed from the dataset ($50 \times 17 = 850$ individual tests). The missing data segments were then filled using the MicroMet preprocessor.

The filled data periods were compared to the original measured data and evaluated for goodness of fit using the Nash–Sutcliffe coefficient (NSC) (Nash and Sutcliffe 1970). The Nash–Sutcliffe analysis of generated (predicted) versus measured (observed) data is provided in Fig. 2. If NSC is 1, then the model is a perfect

fit to the observations. If NSC is between 1 and 0, decreasing values represent a decline in goodness of fit, where 0 represents major deviations between modeled and observed data. Negative NSC values represent results where the fit is poor and the average value of the missing segment represents observations more closely than modeled values. Each box-and-whisker plot in Fig. 2 represents the results of all 50 trials for each missing data span except for the few instances where the randomly selected data period fell too close to the dataset start or finish to perform the ARIMA forecast or backcast.

Figure 2 suggests that the preprocessor does well over short durations of 1–3 days. Many results are satisfactory over longer periods (e.g., up to 6 days), but problems begin to arise as the length of the prediction period increases beyond this value, similar to problems of weather forecasting in general (AMS 1998). Looking at individual cases, periods of weather where there are strong diurnal cycles with relatively stable behavior (in terms of trend, amplitude, etc.) tend to be predictable for extended durations. The preprocessor typically produces a poor fit for periods of highly stochastic behavior or for periods that span different synoptic regimes. Figure 3 shows a series of predictions from a randomly selected start date with durations ranging from 1 through 6 days. The model clearly performs well at short durations (less than 7 days), although problems arise when general model assumptions are not met by the observations (e.g., when no definite diurnal temperature cycle, such as might occur when a cold front passes in midmorning). Even at longer durations, for example, 10 to 21 days (Fig. 4), it can be argued that for some modeling applications, the modeled data with a diurnal cycle would be preferable to a continuous mean value applied across the missing data period. For situations where more than one meteorological station exists within the simulation domain, the MicroMet spatial interpolation scheme (see below) assists in filling large missing data segments.

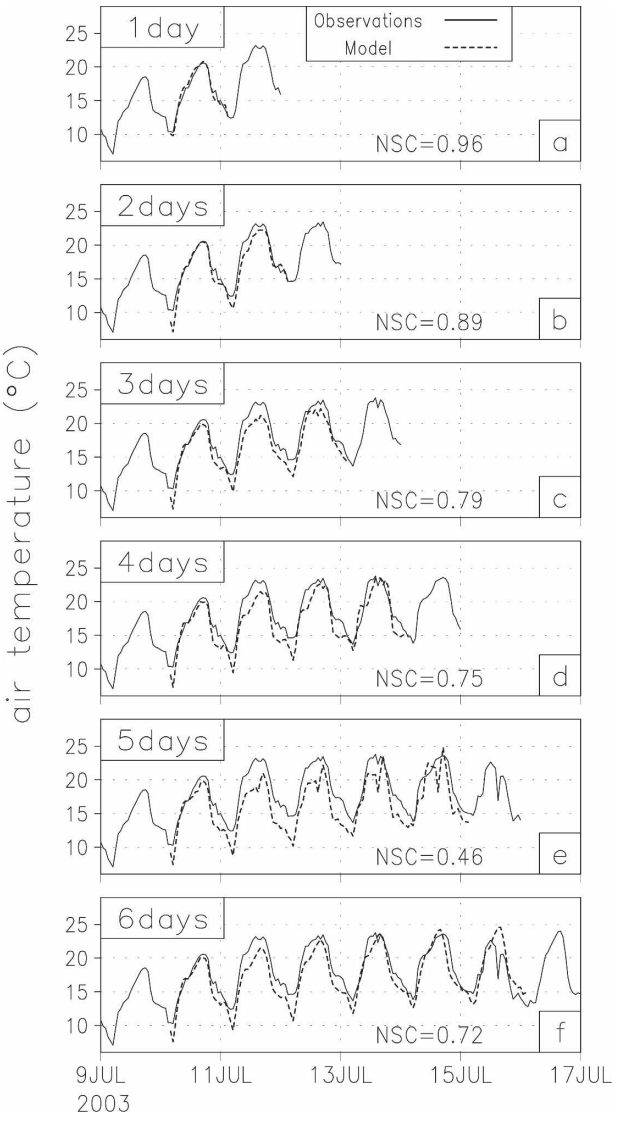

FIG. 3. (a)–(f) Example MicroMet preprocessor air temperature ARIMA data-filling procedure, for the cases of 1–6 days of missing data. Also shown are the NSC values. The relatively poor model performance for the 5-day span in (e) reflects the changing influence period used as part of the ARIMA forecast and backcast.

As highlighted by Fig. 4c, for the case of large missing data segments (e.g., between 7 and 35 days) that are bounded by significantly different trends before and after the missing segment, the ARIMA procedure can lead to a significant misrepresentation within the missing portion (e.g., the model simulation in Fig. 4c is as much as 10°C greater than the observations). Because there is still a need to fill these relatively large missing segments, the MicroMet preprocessor defines two missing-data-span parameters: the first is the maximum span that the ARIMA submodel is to be applied, and the second is the maximum span that is to be filled by the MicroMet preprocessor. Any missing air temperature span falling between these two parameters is filled by calculating the average amplitude of the diurnal cycle before and after the missing period using a data span equal to the missing segment span, and then these two amplitudes are used to create a forecast and backcast that are linearly interpolated across the data gap (Fig. 4d). Our analyses suggest that a value of 3 to 6 is appropriate for the first parameter, and a value of 14 to 28 is appropriate for the second parameter. If these parameters are exceeded, MicroMet leaves the values as missing. Users of the MicroMet preprocessor are

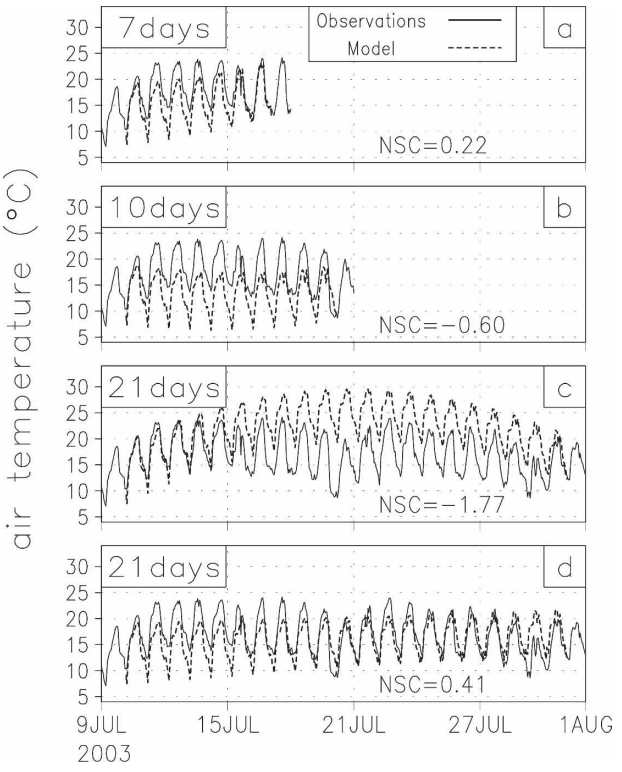

FIG. 4. Example MicroMet preprocessor air temperature ARIMA data-filling procedure, for the cases of (a) 7, (b) 10, and (c) 21 days of missing data. These figures highlight the decreasing skill (decreasing NSC values) in the ARIMA procedure for relatively long missing-data spans. (d) The results of the alternate data-filling procedure suggested for missing-data spans greater than 6 days (see text for details).

encouraged to closely examine their data time series and the resulting filled data segments to assess the validity of the generated data relative to their specific applications.

3. MicroMet model

What follows is a general description of MicroMet (version 1.0), a quasi–physically based, high-resolution (e.g., 30-m to 1-km horizontal grid increment) meteorological distribution model. It is designed specifically to produce high-resolution meteorological forcing distributions required to run spatially distributed terrestrial models over a wide variety of landscapes. The model uses known relationships between meteorological variables and the surrounding landscape (primarily topography) to distribute those variables over any given landscape in computationally efficient and physically plausible ways. MicroMet performs two kinds of adjustments to the available meteorological data: 1) all available data, at a given time, are spatially interpolated over the domain, and 2) physical submodels are applied to each MicroMet variable to improve parameter realism at a given point in space and time. The model distributes fundamental atmospheric forcing variables required to run most terrestrial models: 1) air temperature, 2) relative humidity, 3) wind speed, 4) wind direction, 5) incoming solar radiation, 6) incoming longwave radiation, 7) surface pressure, and 8) precipitation. To calculate these distributions, MicroMet assumes at least one value of each of the following meteorological variables are available at each time step of interest, somewhere within (or near) the simulation domain: air temperature, relative humidity, wind speed, wind direction, and precipitation. For surface pressure and incoming solar and longwave radiation, MicroMet has two options: 1) let the MicroMet submodels create the distributions (in the absence of observations), or 2) merge available observations with the submodel-generated distributions, as part of a data assimilation procedure. This second option produces distributions that match the observations when and where they exist, while accounting for higher-resolution information such as topographic slope and aspect.

a. Spatial interpolation

The model does station (horizontal) interpolations using a Barnes objective analysis scheme (Barnes 1964, 1973; Koch et al. 1983). Objective analysis is the process of interpolating data from irregularly spaced stations to a regular grid. The Barnes scheme applies a Gaussian distance-dependent weighting function, in which the weight that a station contributes to the overall value of the grid point decreases with increasing distance from the point. The interpolation weights, w, are given by

$$w = \exp\left[-\frac{r^2}{f(dn)}\right], \tag{1}$$

where r is the distance between the observation and a grid point, and $f(dn)$ defines a filter parameter whose value ultimately defines how smooth the interpolated field will be. The data spacing and distribution objectively determine the filter parameter value (see Koch et al. 1983).

The Barnes technique employs the method of successive corrections, applying two passes through the station data. Using the weighting function [Eq. (1)] to assign a value to each grid point creates a first-pass analysis field. During the second pass, a difference field is calculated that determines residuals, then, after decreasing the influence radius, a difference correction is applied to the first-pass field. This second pass through the data restores the amplitude of small wavelength

components larger than twice the average observation spacing ($2\Delta n$) suppressed in the first pass. Random errors in the station observations can generate spurious $2\Delta n$ waves (Barnes 1964), so it is important that the scheme filters these from the analysis. Barnes (1973) showed that two passes through the data achieve the desired rapid convergence of the gridded values to the station observations, while providing scale-appropriate resolution.

Since the gridpoint values are weighted averages of the surrounding stations, the gridded values are always less than the maximum and greater than the minimum values surrounding the point, resulting in smoothed station data. When interpolating precipitation, some schemes impose budget-conserving constraints on the applied procedures. While this is appropriate for general interpolation, it is not appropriate for extrapolation into data-poor regions not represented by the available observing stations. MicroMet is designed to perform extrapolation into, for example, mountainous regions where data do not exist, and where the precipitation can be much greater than that measured at the (typically valley) observing sites. For all of the variables, when only one observation exists at a given time step, the Barnes interpolation step is omitted, and MicroMet uniformly distributes the observed value over the domain before performing the MicroMet physically based adjustments, as described below.

b. Meteorological variables

The following descriptions summarize MicroMet procedures implemented to adjust each meteorological variable beyond its initial spatial interpolation. The wind speed and incoming solar and longwave radiation descriptions assume top-of-canopy conditions; adjustments to account for the presence of forest canopies follow Liston and Elder (2005, manuscript submitted to *J. Hydrometeor.*).

1) AIR TEMPERATURE

Historically, simple interpolation routines (e.g., Burrough and McDonnell 2000) have been used to spatially distribute point air temperature data. While these methods work in flat terrain, they often misrepresent temperature distributions in areas having significant topographic variability. Recent studies have tried to improve the simulated temperature distributions by taking advantage of the strong temperature–elevation relationships that are known to exist. Dodson and Marks (1997) summarize two of the most realistic and general methods used to distribute point air temperature data over mountainous terrain: assuming 1) neutral atmospheric stability, and 2) a constant linear lapse rate. They conclude that the constant linear lapse rate method most successfully reproduces the natural environment, but also note that lapse rates can vary widely over space and time. In MicroMet, this deficiency is constrained by defining air temperature lapse rates that vary monthly throughout the year. Alternatively, the MicroMet can utilize user-defined lapse rate data.

First, the station air temperatures are adjusted to a common level, using the formula

$$T_0 = T_{\text{stn}} - \Gamma(z_0 - z_{\text{stn}}), \tag{2}$$

where T_{stn} (°C) is the observed station air temperature at the station elevation, z_{stn} (m); T_0 (°C) is the air temperature at the reference elevation, z_0 (m) (sea level, or $z_0 = 0.0$, is used in MicroMet); and the lapse rate, Γ (°C m^{-1}), is given in Table 1 and varies depending on the month of the year (Kunkel 1989) or calculated based on adjacent station data.

The reference-level station temperatures are then interpolated to the model grid using the Barnes objective analysis scheme (Koch et al. 1983). The gridded topography data and Table 1 (or observed) lapse rate are then used to adjust the reference-level gridded temperatures to the elevations provided by the topography dataset, using

$$T = T_0 - \Gamma(z - z_0), \tag{3}$$

where T_0 is now the gridded air temperature at the reference elevation, z_0, and T (°C) is the gridded air temperature at the elevation of the topographic dataset, z (m).

2) RELATIVE HUMIDITY

Since relative humidity is a nonlinear function of elevation, the relatively linear dewpoint temperature is

TABLE 1. Air temperature lapse rate variations, for each month of the year, in the Northern Hemisphere (Kunkel 1989), and precipitation–elevation adjustment factors (Thornton et al. 1997).

Month	Air temperature lapse rate (°C km^{-1})	Vapor pressure coefficient (km^{-1})	Precipitation adjustment factor (km^{-1})
Jan	4.4	0.41	0.35
Feb	5.9	0.42	0.35
Mar	7.1	0.40	0.35
Apr	7.8	0.39	0.30
May	8.1	0.38	0.25
Jun	8.2	0.36	0.20
Jul	8.1	0.33	0.20
Aug	8.1	0.33	0.20
Sep	7.7	0.36	0.20
Oct	6.8	0.37	0.25
Nov	5.5	0.40	0.30
Dec	4.7	0.40	0.35

used for the elevation adjustments. First, we convert the station relative humidity, RH (%), to dewpoint temperature, T_d (°C), using the air temperature, T (°C). The saturation vapor pressure, e_s (Pa), at temperature T is

$$e_s = a \exp\left(\frac{bT}{c + T}\right), \tag{4}$$

where for water $a = 611.21$ Pa, $b = 17.502$, and $c = 240.97$°C, and for ice $a = 611.15$ Pa, $b = 22.452$, and $c = 272.55$°C (Buck 1981). Using Eq. (4), the RH equation

$$\mathrm{RH} = 100 \frac{e}{e_s} \tag{5}$$

can be solved for the actual vapor pressure, e (Pa). The dewpoint temperature can then be calculated from

$$T_d = \frac{c \ln(e/a)}{b - \ln(e/a)}. \tag{6}$$

Now the dewpoint temperatures at the stations can be adjusted to a common reference level using Eq. (2), where the temperatures are now dewpoint temperatures and the lapse rate is the dewpoint temperature lapse rate, Γ_d (°C m^{-1}) (Kunkel 1989),

$$\Gamma_d = \lambda \frac{c}{b}, \tag{7}$$

where λ (m^{-1}) is a vapor pressure coefficient (Table 1) that varies during each month of the year (Kunkel 1989).

The reference-level station dewpoint temperatures are then interpolated to the model grid using the Barnes objective analysis scheme (Koch et al. 1983). The T_d lapse rate is used to take the reference-level gridded values to the actual topographic elevations using an equation similar to Eq. (3), where now the temperatures are dewpoint temperatures, and the lapse rate is the dewpoint temperature lapse rate. These gridded dewpoint temperature values are then converted to RH using Eqs. (4) and (5), where e is calculated by substituting T_d for T in Eq. (4).

3) Wind speed and direction

Because of the problems with interpolating over the 360°/0° direction line, station wind speed, W (m s^{-1}), and direction, θ, values are first converted to zonal, u (m s^{-1}), and meridional, v (m s^{-1}), components using

$$u = -W \sin(\theta), \tag{8}$$

$$v = -W \cos(\theta). \tag{9}$$

The u and v components are then independently interpolated to the model grid using the Barnes objective analysis scheme (Koch et al. 1983). The resulting values are converted back to speed and direction using

$$W = (u^2 + v^2)^{(1/2)}, \tag{10}$$

$$\theta = \frac{3\pi}{2} - \tan^{-1}\left(\frac{v}{u}\right), \tag{11}$$

where north has a direction of zero.

These gridded speed and direction values are modified using a simple, topographically driven wind model, following Liston and Sturm (1998) that adjusts the speeds and directions according to topographic slope and curvature relationships. To perform the wind modification calculations, the topographic slope, topographic slope azimuth, and topographic curvature must be computed. The terrain slope, β, is given by

$$\beta = \tan^{-1}\left[\left(\frac{\partial z}{\partial x}\right)^2 + \left(\frac{\partial z}{\partial y}\right)^2\right]^{(1/2)}, \tag{12}$$

where z (m) is the topographic height, and x (m) and y (m) are the horizontal coordinates. The terrain slope azimuth, ξ, with north having zero azimuth, is

$$\xi = \frac{3\pi}{2} - \tan^{-1}\left(\frac{\partial z/\partial y}{\partial z/\partial x}\right). \tag{13}$$

The curvature, Ω_c, is computed at each model grid cell by first defining a curvature length scale or radius, η (m), that defines the topographic length scale to be used in the curvature calculation. This length scale is equal to approximately half the wavelength of the topographic features within the domain (e.g., the distance from a typical ridge to the nearest valley).

For each model grid cell, the curvature is calculated by taking the difference between that grid cell elevation, and the average elevations of the two opposite grid cells a length scale distance from that grid cell. This difference is calculated for each of the opposite directions S–N, W–E, SW–NE, and NW–SE from the main grid cell (effectively obtaining a curvature for each of the four direction lines), and the resulting four values are averaged to obtain the curvature. Thus,

$$\Omega_c = \frac{1}{4}\left[\frac{z - 1/2(z_W + z_E)}{2\eta} + \frac{z - 1/2(z_S + z_N)}{2\eta} + \frac{z - 1/2(z_{SW} + z_{NE})}{2\sqrt{2}\eta} + \frac{z - 1/2(z_{NW} + z_{SE})}{2\sqrt{2}\eta}\right], \tag{14}$$

where z_W, z_{SE}, etc. are the elevation values for the grid cell at approximately curvature length scale distance, η,

in the corresponding direction from the main grid cell. To simplify applying this distribution in the topographic weighting function described below, the curvature is then scaled such that $-0.5 \leq \Omega_c \leq 0.5$ over the simulation domain.

The slope in the direction of the wind, Ω_s, is

$$\Omega_s = \beta \cos(\theta - \xi). \quad (15)$$

This Ω_s is also scaled such that $-0.5 \leq \Omega_s \leq 0.5$ over the simulation domain.

The wind weighting factor, W_w, used to modify the wind speed is given by (Liston and Sturm 1998)

$$W_w = 1 + \gamma_s \Omega_s + \gamma_c \Omega_c, \quad (16)$$

where γ_s and γ_c are the slope weight and curvature weight, respectively. The Ω_s and Ω_c values range between -0.5 and $+0.5$. Valid γ_s and γ_c values are between 0 and 1, with values of 0.5 giving approximately equal weight to slope and curvature. It is suggested that Ω_s and Ω_c be set such that $\Omega_s + \Omega_c = 1.0$. This constraint will limit the total wind weight to between 0.5 and 1.5, but this is not actually required by the model implementation.

Finally, the terrain-modified wind speed, W_t (m s^{-1}), is calculated from

$$W_t = W_w W. \quad (17)$$

The wind directions are modified by a diverting factor, θ_d, according to Ryan (1977),

$$\theta_d = -0.5 \Omega_s \sin[2(\xi - \theta)]. \quad (18)$$

This diverting factor is added to the wind direction to yield the terrain-modified wind direction, θ_t,

$$\theta_t = \theta + \theta_d. \quad (19)$$

The resulting speeds, W_t, and directions, θ_t, are converted to u and v components using Eqs. (8) and (9).

The wind model was tested against an observational dataset (Pohl et al. 2005, manuscript submitted to *Arct. Antarct. Alp. Res.,* hereafter PML) from Trail Valley Creek, a research basin located in the Northwest Territories, Canada, at 68°45′N, 133°30′W. The observations include wind speed and direction data (15-min averages) from six towers located on and around a low hill (approximately 50-m high) in the northwestern part of the basin (Fig. 5a).

The following approach was used to define reasonable values of γ_s and γ_c. First, the wind data were binned into the eight principal wind directions (N, NE, E, etc.), and W in Eq. (17) was defined to be the average wind speed of the six stations, for each directional bin, at each observation time. Second, we reasoned that, for northerly and southerly winds, the topographic

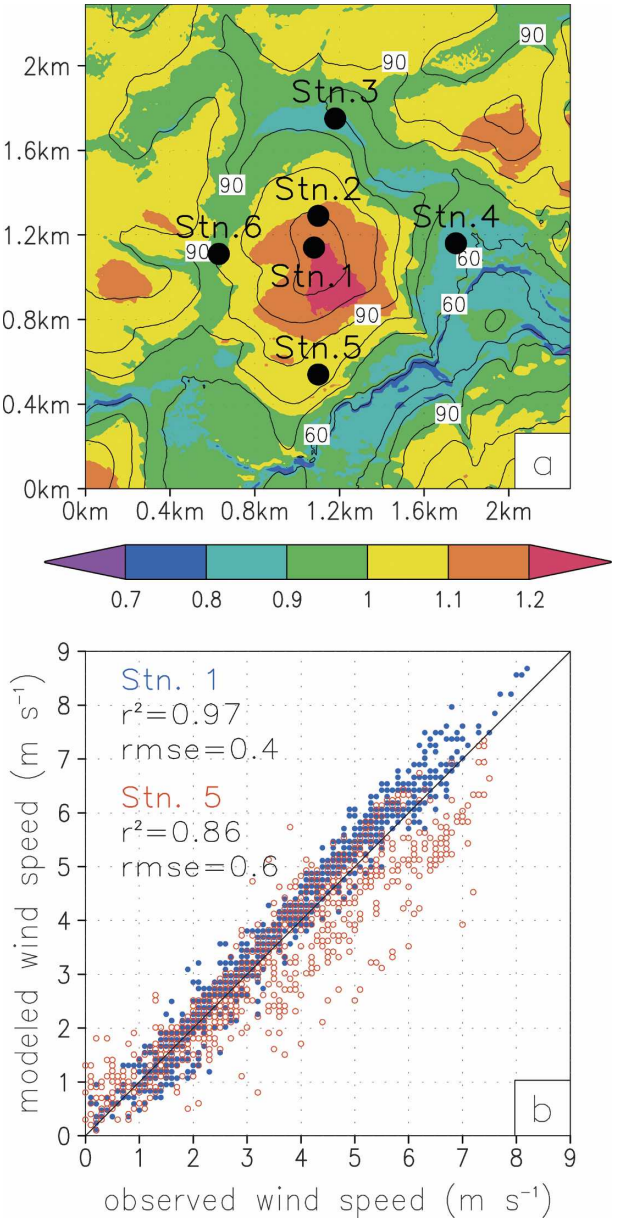

FIG. 5. (a) Simulation domain topography (contour interval 10 m), wind weighting factor (color shades), and meteorological station locations (adapted following PML). (b) Comparison of modeled and observed wind speed for stations 1 and 5, for both northerly and southerly winds; included are the square of the linear correlation coefficient, r^2, and rmse (n = 919).

slope at stations 1 and 3 were zero (Fig. 1a). For this case, the second term on the right-hand side of Eq. (16) is zero. Using this, and by defining W_t to be equal to the station observations, Eqs. (16) and (17) were combined to yield γ_c as the only unknown. The resulting equation was solved for stations 1 and 3, using both northerly and southerly winds (n = 919), and an average γ_c was calculated. This γ_c value was then applied to Eq. (16) and

the process was repeated to calculate the γ_s for stations 2 and 5 (which have both slope and curvature). The resulting values ($n = 919$) were combined to yield an average γ_s. The ratio of calculated γ_c to γ_s equaled 0.72, which, under the assumption that γ_s and γ_c sum to unity, yielded $\gamma_s = 0.58$ and a $\gamma_c = 0.42$.

These values were implemented in the wind model and used to simulate the wind flow over the hill (Fig. 5a). Comparison of the simulated wind speeds and the observations at stations 1 and 5, for both northerly and southerly winds, is presented in Fig. 5b. Figure 5a also displays the W_w distribution for the case of southerly winds. Shown are the relatively higher weighting values on ridge tops and windward slopes, and lower values on lee slopes and in valley bottoms. PML provided a more complete comparison of the model and wind observations.

4) SOLAR RADIATION

The following equations use the model time to calculate the solar radiation for that specific time. In addition, they consider the influence of cloud cover, direct and diffuse solar radiation, and topographic slope and aspect on incoming solar radiation.

Cloud cover is estimated by first taking the surface gridded T and T_d fields described in sections 3b(1) and 3b(2) and the associated lapse rates to calculate T and T_d for the 700-mb level of the atmosphere. These T and T_d surfaces are then used to calculate the relative humidity at 700 mb, RH_{700}, using Eqs. (4) and (5).

Following Walcek (1994), and assuming a minimum averaging dimension, this RH_{700} distribution is used to define the cloud fraction, σ_c,

$$\sigma_c = 0.832 \exp\left(\frac{\mathrm{RH}_{700} - 100}{41.6}\right) \qquad (0 \le \sigma_c \le 1). \tag{20}$$

An illustration of this relationship is given in Fig. 6.

Solar radiation striking earth's surface, Q_{si} (W m^{-2}), including the influence of sloping terrain, is given by

$$Q_{\mathrm{si}} = S^*(\Psi_{\mathrm{dir}} \cos i + \Psi_{\mathrm{dif}} \cos Z), \tag{21}$$

where the angle between direct solar radiation and a sloping surface is given by i, and assuming that diffuse radiation impinges upon an area corresponding to a horizontal surface. The solar irradiance at the top of the atmosphere striking a surface normal to the solar beam is given by S^* (=1370 W m^{-2}; Kyle et al. 1985), and Ψ_{dir} and Ψ_{dif} are the direct and diffuse, respectively, net sky transmissivities, or the fraction of solar radiation reaching the surface.

The solar zenith angle, Z, is

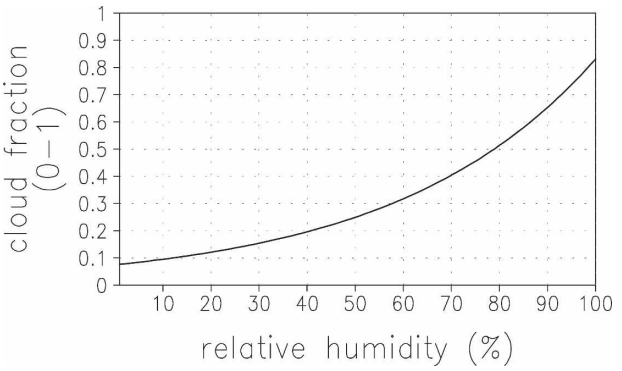

FIG. 6. Cloud-cover fraction as a function of MicroMet-calculated 700-mb relative humidity.

$$\cos Z = \sin\delta \sin\phi + \cos\delta \cos\phi \cos\tau, \tag{22}$$

where ϕ is latitude, and τ is the hour angle measured from local solar noon,

$$\tau = \pi\left(\frac{h}{12} - 1\right), \tag{23}$$

where h is the hour of the day. The solar declination angle, δ, is approximated by

$$\delta = \phi_T \cos\left[2\pi\left(\frac{d - d_r}{d_y}\right)\right], \tag{24}$$

where ϕ_T is the latitude of the tropic of Cancer, d is the day of the year, d_r is the day of the summer solstice, and d_y is the average number of days in a year.

The angle i is given by

$$\cos i = \cos\beta \cos Z + \sin\beta \sin Z \cos(\mu - \xi_s), \tag{25}$$

and the terrain slope, β, is given by Eq. (12). The terrain slope azimuth now requires south to have zero azimuth, ξ_s, so Eq. (13) is used where the first term on the right-hand-side is now $\pi/2$. The solar azimuth, μ, with south having zero azimuth, is given by

$$\mu = \sin^{-1}\left(\frac{\cos\delta \sin\tau}{\sin Z}\right). \tag{26}$$

To account for scattering, absorption, and reflection of solar radiation by clouds, the solar radiation is scaled according to (Burridge and Gadd 1974)

$$\Psi_{\mathrm{dir}} = (0.6 - 0.2 \cos Z)(1.0 - \sigma_c) \tag{27}$$

for direct solar radiation and

$$\Psi_{\mathrm{dif}} = (0.3 - 0.1 \cos Z)\sigma_c \tag{28}$$

for diffuse solar radiation, where σ_c represents the cloud-cover fraction given by Eq. (20).

If incoming solar radiation observations are available, they can be combined with the solar radiation

model as part of a data assimilation procedure. Here the point observations are compared with the model-distributed field at the corresponding model grid cells. The differences between the observations and modeled values are computed, and a gridded surface is generated through those differences using the Barnes analysis scheme. The difference field is then added to the model-distributed field. This produces distributions that match the observations when and where they exist, while including the higher-resolution information provided by the modeled distributions.

The solar radiation model was compared against observations provided by the CLPX. Figure 7a provides an analysis of modeled and observed hourly incoming solar radiation data from the CLPX Walton Creek meteorological station, spanning the time 23 September 2002 through 27 September 2003. The model yielded an r^2 value of 0.87 for the hourly data, and captured the observed seasonal variations (Fig. 7b).

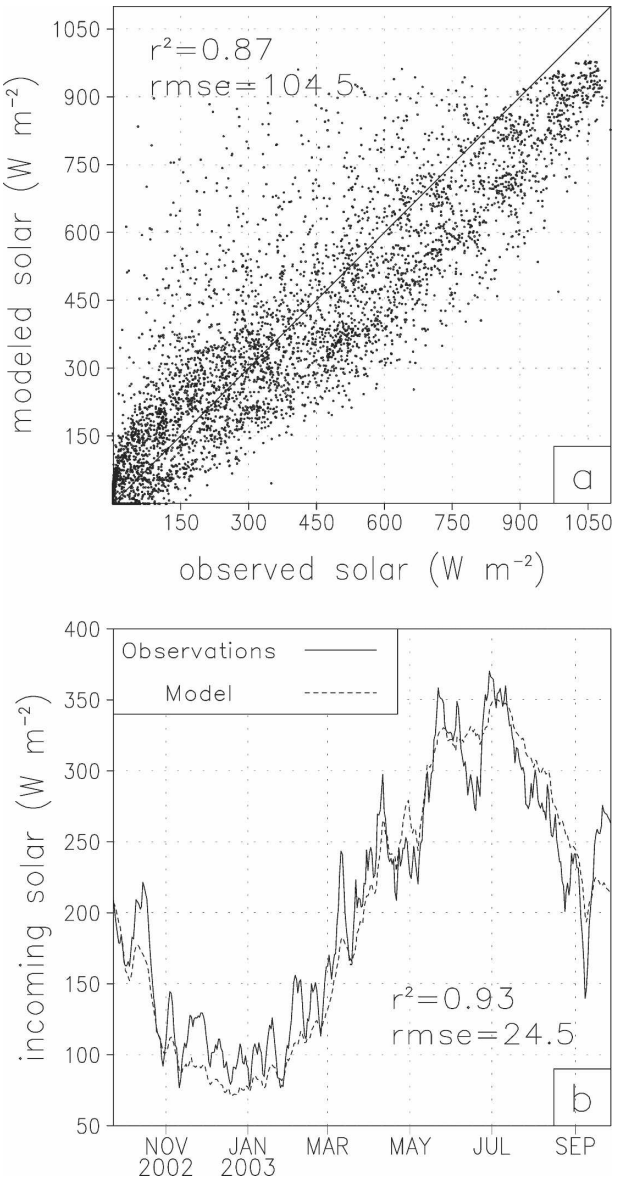

FIG. 7. Incoming solar radiation data from the NASA CLPX Walton Creek meteorological station, 23 Sep 2002–27 Sep 2003 (n = 8880). (a) Comparison of hourly modeled and observed data; the thin scattering of high-solar-radiation values compared to the observations is the result of frost and snow on the sensor, etc., that are not accounted for in the model. (b) Time evolution of daily average modeled and observed solar radiation. To improve visualization, a 7-day running mean was applied to the daily data.

5) LONGWAVE RADIATION

Incoming longwave radiation is calculated while taking into account cloud cover and elevation-related variations following Iziomon et al. (2003). Incoming longwave radiation reaching earth's surface, Q_{li} (W m^{-2}), is given by

$$Q_{\mathrm{li}} = \varepsilon\sigma T^4, \tag{29}$$

where σ is the Stefan–Boltzmann constant, and T (K; note the change in units) is the air temperature. The atmospheric emissivity, ε, is

$$\varepsilon = \kappa(1 + Z_s\sigma_c{}^2)[1 - X_s \exp(-Y_s e/T)], \tag{30}$$

where e (Pa) is the atmospheric vapor pressure, and the coefficients X_s, Y_s, and Z_s depend on elevation according to

$$\begin{aligned} C_s &= C_1 && z < 200 \\ C_s &= C_1 + (z - z_1)\left(\frac{C_2 - C_1}{z_2 - z_1}\right) && 200 \le z \le 3000, \\ C_s &= C_2 && 3000 < z \end{aligned} \tag{31}$$

where z (m) is the elevation of the land surface, and X, Y, and Z can be substituted for C, with $X_1 = 0.35$, $X_2 = 0.51$, $Y_1 = 0.100$ K Pa^{-1}, $Y_2 = 0.130$ K Pa^{-1}, $Z_1 = 0.224$, $Z_2 = 1.100$, $z_1 = 200$ m, and $z_2 = 3000$ m. These coefficients represent a combination of those defined by Iziomon et al. (2003) for elevations below 1500 m; X_2 and Y_2 were determined by increasing the Iziomon et al. (2003) coefficients linearly to 3000 m; and Z_2 and $\kappa = 1.083$ were adjusted to create a best fit to CLPX observational datasets.

Comparison of longwave radiation simulations with CLPX Walton Creek observations (Fig. 8) yielded results similar in quality to those in the solar radiation comparison. If incoming longwave radiation observations are available, they can be combined with the long-

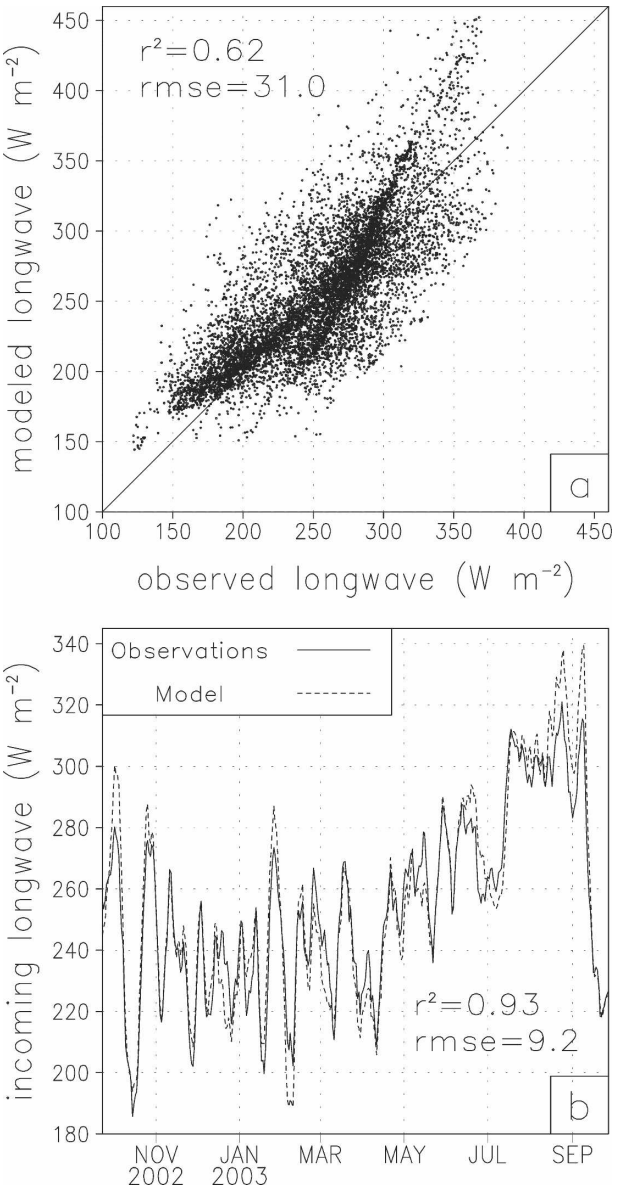

FIG. 8. Incoming longwave radiation data from the NASA CLPX Walton Creek meteorological station, 23 Sep 2002–27 Sep 2003 ($n = 8880$). (a) Comparison of hourly modeled and observed data. (b) Time evolution of daily average modeled and observed longwave radiation. To improve visualization, a 7-day running mean was applied to the daily data.

wave radiation model as part of the data assimilation procedure described in section 3b(4).

6) SURFACE PRESSURE

In the absence of surface pressure observations, a time-independent atmospheric pressure, p, distribution is given by

$$p = p_0 \exp\left(-\frac{z}{H}\right), \tag{32}$$

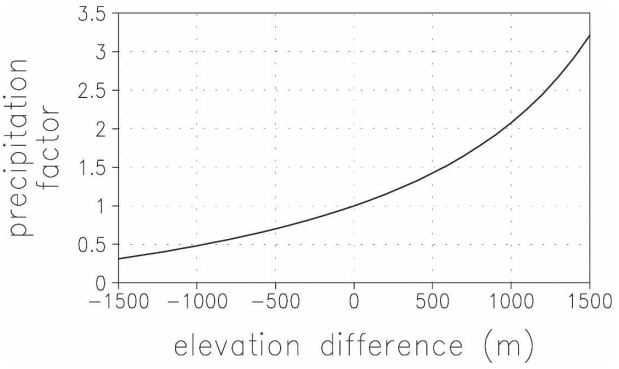

FIG. 9. Dependence of the precipitation-adjustment factor on the elevation difference between the precipitation observing stations and a specific grid cell, for $\chi = 0.35$ km^{-1} (a winter value).

where p_0 is a reference sea level pressure (101 300 Pa), and H is the scale height of the atmosphere (≈8000 m) (Wallace and Hobbs 1977). If surface pressure observations are available, they can be combined with the surface pressure model as part of the data assimilation procedure described in section 3b(4).

7) PRECIPITATION

To distribute precipitation over the domain, observed precipitation values are first interpolated to the model grid using the Barnes objective analysis scheme. To generate a topographic reference surface, the station elevations are also interpolated to the model grid. The reason interpolated station elevations are used as the topographic reference surface, as opposed to a reference like sea level, is that the precipitation adjustment function is a nonlinear function of elevation difference. The modeled liquid-water precipitation rate, P (mm h^{-1}), is computed from

$$P = P_0\left[\frac{1 + \chi(z - z_0)}{1 - \chi(z - z_0)}\right], \tag{33}$$

where P_0 is the interpolated station precipitation, z_0 is the interpolated station elevation surface, and χ (km^{-1}) is a factor (Table 1) defined to vary seasonally (monthly values) (Thornton et al. 1997). Figure 9 illustrates how the precipitation adjustment function [the term in brackets to the right of P_0 in Eq. (33)] varies with elevation difference for $\chi = 0.35$ km^{-1} (a winter value). Since χ is expected to vary geographically, MicroMet allows the user to modify its monthly values from those listed in Table 1.

4. Example MicroMet simulations

To test the overall MicroMet implementation, the model was run for one year starting on 1 September

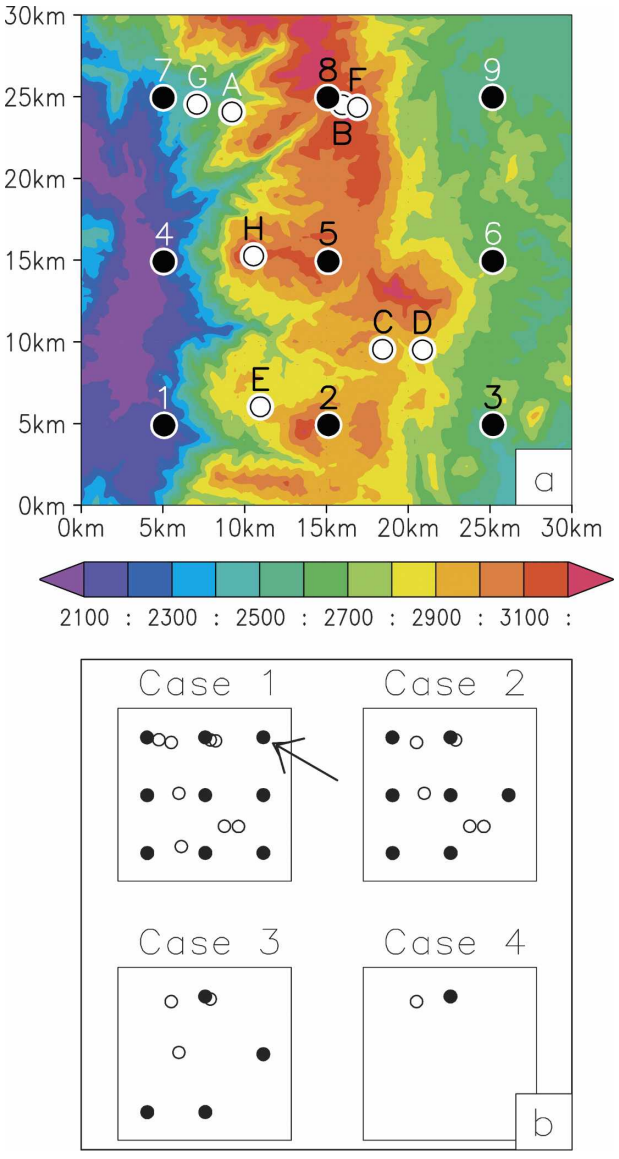

FIG. 10. (a) Colorado simulation domain and topography (m), and meteorological data sites comprised of LAPS atmospheric analysis data (black dots) and meteorological stations (white dots). Table 2 provides site descriptions. (b) Data sites used in the four model simulations: cases 1, 2, 3, and 4 included 17, 12, 7, and 2 sites, respectively.

2002, over a 30 km by 30 km area, using an hourly time step and 200-m grid increment (Fig. 10a). The simulation domain covered the CLPX Rabbit Ears mesocell study area located at 40°27′N, 106°22′W in north-central Colorado (Cline et al. 2005, manuscript submitted to *J. Hydrometeor.*), and is characterized by moderate topographic relief. Meteorological data for the simulations included a collection of gridded atmospheric analyses data (nine grid points) from the National Oceanic and Atmospheric Administration's (NOAA) Local Analysis and Prediction System (LAPS) (Liston et al. 2005, manuscript submitted to *J. Hydrometeor.*) and eight independent meteorological station datasets provided from a variety of sources (Table 2; Fig. 10a).

Four simulations were performed: case 1 used all of the available meteorological data, data from 17 sites; case 2 used 12 sites; case 3 used 7 sites; and case 4 used 2 sites. The site elimination order was determined randomly, and the resulting distributions are shown in Fig. 10b.

An initial requirement of the model is that it closely reproduces the observations at the observation point. Figure 11a compares the hourly station 9 temperature observations (n = 8760) with the model simulation at the coincident model grid point. Also shown is a comparison of the observations with the case 4 simulation at that grid point. Figure 11b displays the daily average temperature evolution of the observations, case 1, and case 4. The model behaves as expected.

A second requirement is that the model produces reasonable spatial distributions of the modeled variables, and that these distributions maintain their viability as the number of meteorological observations is reduced. Figure 12a shows the simulated January-average air temperature, and Fig. 12b shows case 4 minus case 1 for this field. The reduction of observing sites from 17 to 2 yields January-average temperature differences of 1°C or less. Looking at the hourly data that make up this figure shows that the individual fields have similar differences (the Fig. 12b difference field is not the result of larger positive and negative hourly values canceling each other). The Fig. 12b spatial pattern is the result of two factors. First, the differences are greatest along the eastern and western areas of the domain. These are areas of greatest elevation change between the two remaining case 4 data locations (A and 8, in Fig. 10a) and the simulation domain topography (Fig. 10a). Therefore, the simulated distributions in these areas are strongly dependent upon model factors such as the assumed lapse rate. Second, since the case 4 data locations are relatively near to each other, there is little regional information contained in the case 4 simulation. This leads to a difference field with a change of sign from the east to the west part of the domain (to reproduce the case 1 simulation using only case 4 data, different lapse rates would have to be applied to the east and west parts of the domain).

Figures 13a and 13b provide the same information as Fig. 12, but for relative humidity. In addition to the reasons for the Fig. 12b spatial pattern, the dependence of relative humidity on temperature leads to a similar relative humidity difference field (Fig. 13b).

TABLE 2. Meteorological data sites used in the spatially distributed model simulations (Fig. 10).

Station ID	Site description	Easting (m)	Northing (m)	Elevation (m)	Variables[a]
A	Buffalo Pass-CLPX	351 126	487 974	2804	*T*, *R*, *W*, *D*
B	Spring Creek-CLPX	357 887	488 407	3233	*T*, *R*, *W*, *D*
C	Walton Creek-CLPX	360 335	473 447	2950	*T*, *R*, *W*, *D*
D	Columbine-SNOTEL[b]	362 779	473 410	2794	*T*
E	Rabbit Ears-SNOTEL	352 863	469 933	2911	*T*
F	Tower-SNOTEL	358 815	488 253	3219	*T*
G	Dry Lake-RAWS[c]	348 990	488 445	2515	*T*, *R*
H	Storm Peak Laboratory-DRI[d]	352 450	479 159	3210	*T*, *R*, *W*, *D*
1	LAPS	346 979	468 801	2477	*T*, *R*, *W*, *D*, *P*
2	LAPS	357 033	468 819	2837	*T*, *R*, *W*, *D*, *P*
3	LAPS	367 086	468 831	2714	*T*, *R*, *W*, *D*, *P*
4	LAPS	346 955	478 818	2430	*T*, *R*, *W*, *D*, *P*
5	LAPS	357 017	478 837	2852	*T*, *R*, *W*, *D*, *P*
6	LAPS	367 075	478 848	2782	*T*, *R*, *W*, *D*, *P*
7	LAPS	346 933	488 842	2573	*T*, *R*, *W*, *D*, *P*
8	LAPS	356 999	488 861	2913	*T*, *R*, *W*, *D*, *P*
9	LAPS	367 067	488 873	2704	*T*, *R*, *W*, *D*, *P*

[a] Meteorological variables available at each site: T = air temperature, R = relative humidity, W = wind speed, D = wind direction, and P = precipitation.
[b] SNOTEL = snow telemetry.
[c] RAWS = Remote Automated Weather Station.
[d] DRI = Desert Research Institute.

The r^2 and root-mean-square-error (rmse) calculations displayed in Figs. 12 and 13 were also performed for cases 2 and 3, and for July; the results are presented in Table 3.

An analysis of the time evolution of domain-average air temperature (Fig. 14) and relative humidity (Fig. 15) was also performed. Table 4 presents the statistical information from these simulations. The figures and table highlight the general decrease in simulation quality as the number of data sites is reduced. The reduction from 17 to 2 stations produced a change in rmse values from 0.1° to 0.8°C and 0.6% to 5.5%, for air temperature and relative humidity, respectively.

5. Discussion

a. Applications

MicroMet's development was necessary to define physically appropriate atmospheric forcings to drive a wide variety of terrestrial (e.g., hydrology and ecosystem) models. Historically, this merging of atmospheric and hydrologic sciences has been hampered by the inherent mismatch in spatial scales between the two disciplines. Atmospheric scientists have studied the atmosphere at global, synoptic, and regional scales. Their models typically have a strong focus on the atmospheric dynamics occurring over these scales and, as such, the models have been formulated to operate on grid increments spanning from roughly 100-km (global) to 1-km (regional) grid increments.

In contrast, hydrologic models have generally operated over well-defined watersheds using grid increments ranging from 30 m to 1 km. Models used to simulate hydrologic processes usually include moisture flow dynamics and descriptions of physical and vegetation-related processes that influence moisture transport within the basin and associated interactions with the atmosphere. To realistically (physically) represent these basin moisture-transport processes, terrestrial models are required to run at grid increments as small as 30 m. Thus, there is a significant mismatch in scales between atmospheric and terrestrial approaches.

MicroMet was developed to serve as an interface between the relatively coarse-resolution atmospheric data (available as either station observations and/or gridded atmospheric data, e.g., 1–100-km grid increment) and fine-resolution (e.g., 30-m to 1-km grid increment) hydrological and ecological models. This lack of available high-resolution atmospheric forcing data has hindered the development of spatially and physically realistic hydrologic and ecologic models. Evidence of this can be found by looking at the growth of intermediate-scale (e.g., 10–15-km grid increment) land surface hydrology models over the last 10–15 yr (Wood et al. 1997; Mitchell et al. 2004). These models have commonly had to adopt the atmospheric modeling approach of "parameterizing" the subgrid-scale physics within the terrestrial system they are attempting to model. MicroMet converts available atmospheric forcing data to the sufficiently high spatial resolution re-

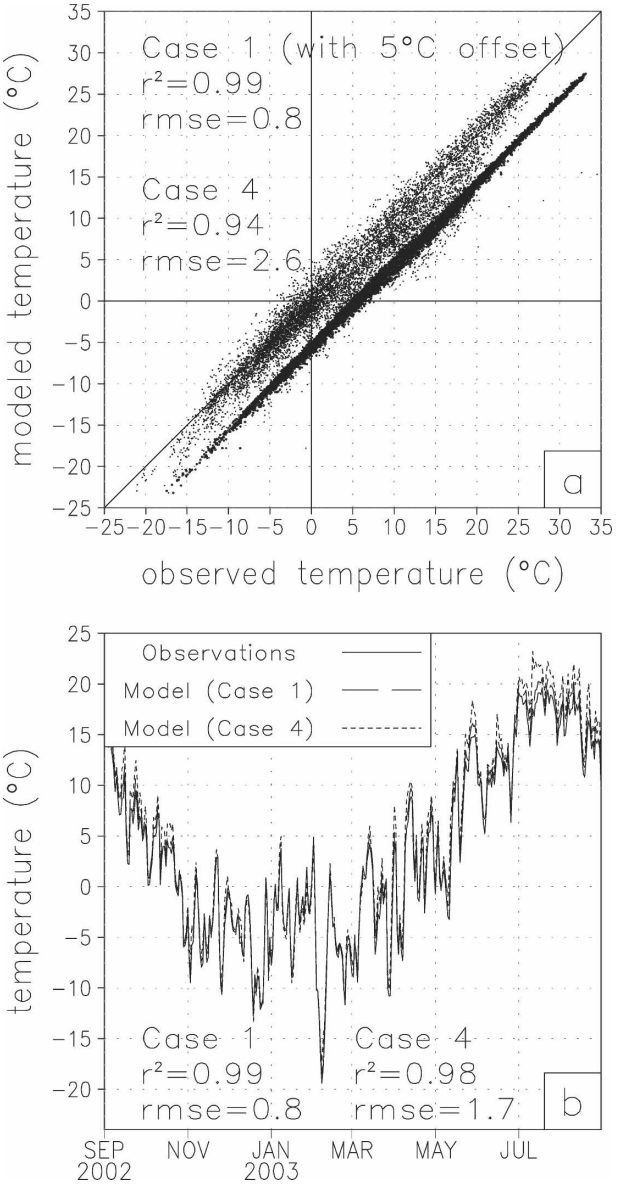

FIG. 11. (a) Comparison of station 9 (see arrow in Fig. 10b) hourly air temperature observations with case 1 and case 4 model simulations at the corresponding grid point (n = 8760). Case 1 has been offset by 5°C to help distinguish those data from the case 4 data. (b) Comparison of station 9 daily average observations with case 1 and case 4 model simulations.

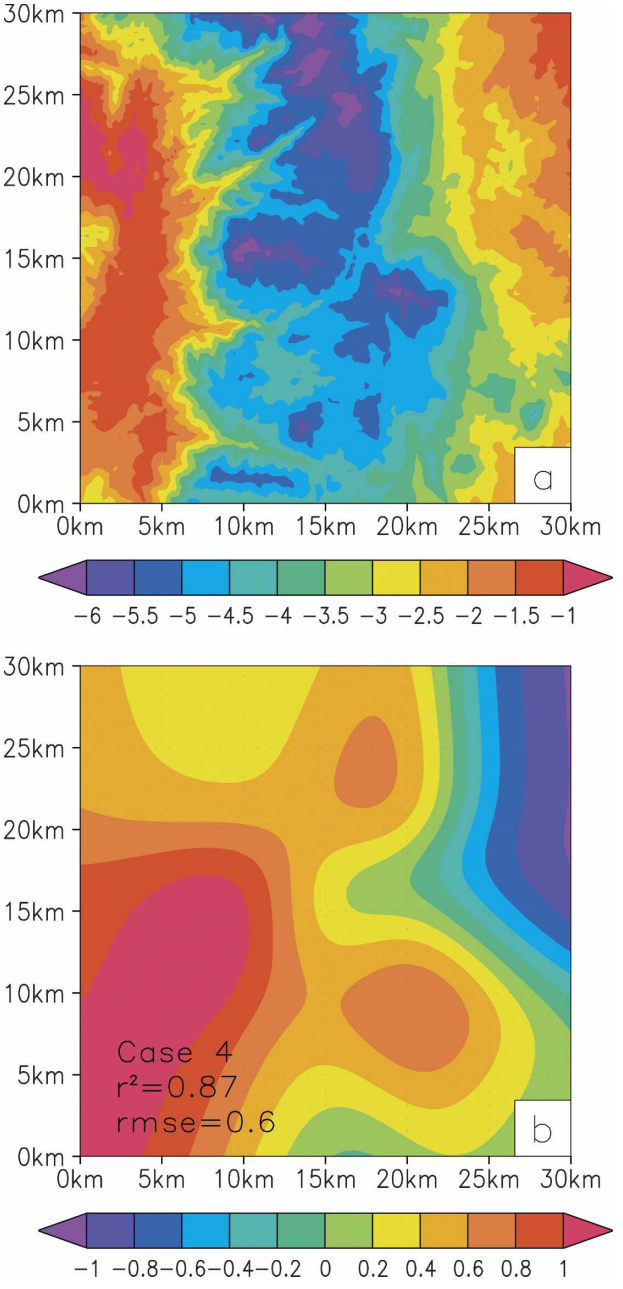

FIG. 12. (a) Case 1 simulated January-average air temperature (°C), and (b) case 4 minus case 1 for this field.

quired to drive terrestrial process models operating at realistic spatial scales.

b. Limitations

As part of our MicroMet development, we recognized many limitations in the model formulation. Two things are clear from the preceding MicroMet description: 1) the finescale adjustments to the observed or analyzed meteorological fields are largely driven by simple topographic relationships, and 2) the adjustments are completely one-way. This one-way coupling means there are no feedbacks between the land and atmosphere in the calculations of the near-surface atmospheric conditions. We also understand that land surface conditions can have a substantial impact on near-surface atmospheric properties (Pielke 2001). Thus, there is an opportunity for additional improved physical realism in the MicroMet spatial interpolations

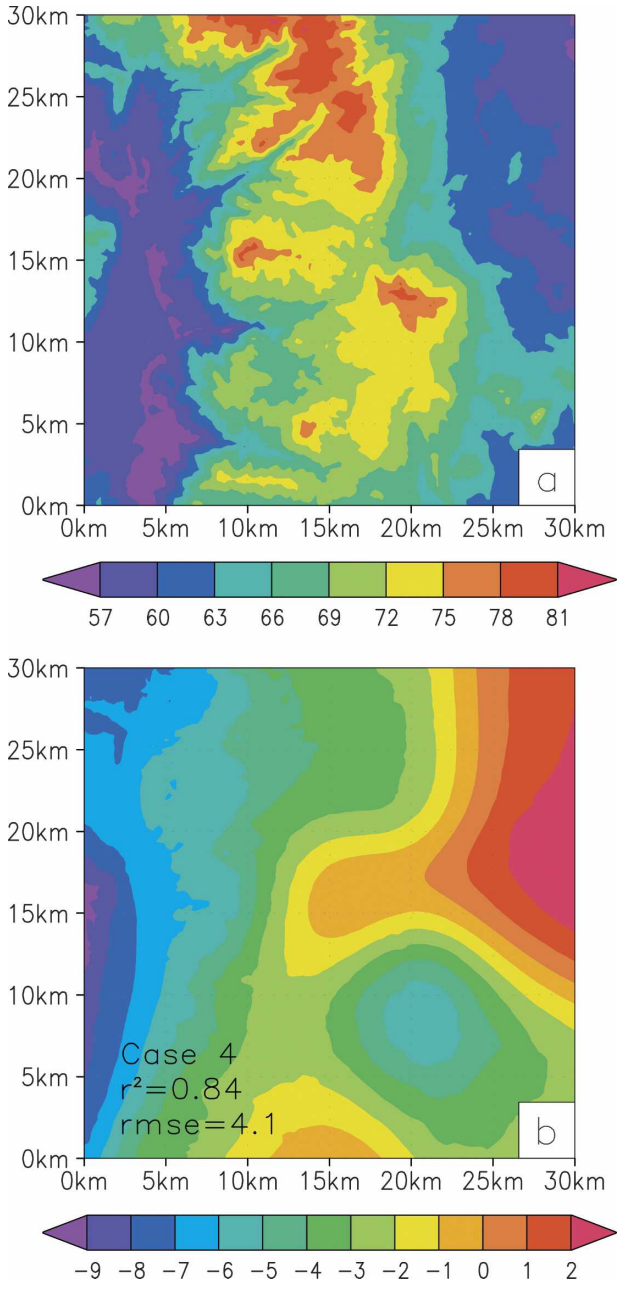

FIG. 13. (a) Case 1 simulated January-average relative humidity (%), and (b) case 4 minus case 1 for this field.

and distributions. We use three examples to illustrate why the MicroMet approaches are an oversimplification of the natural system, and suggest how later versions of MicroMet might be modified to correct those limitations.

1) WET VERSUS DRY SOIL

Consider a flat domain with one meteorological tower observation. MicroMet will distribute the tower temperature observation to be constant over the domain. This distribution is probably appropriate under conditions of constant soil moisture and uniform vegetation type, but, to consider a more realistic example, let us assume that part of the domain is dry and another part is wet. In this case, we expect the underlying surface will influence the resulting air temperature (the air above the drier surface will be warmer, while that above the wetter surface will be cooler). To account for this variability, MicroMet could calculate a surface energy budget under the assumption that the air temperatures above the two surfaces are initially the same (but the soil moistures are different), and then use the resulting sensible and latent heat fluxes to adjust the assumed air temperatures. Note that implementing these enhancements requires coupling MicroMet to an energy-balance/land surface hydrology model, thus significantly increasing the complexity, and potentially increasing the biases, of the current modeling system.

TABLE 3. Statistical information (square of the linear correlation coefficient, r^2, and rmse) corresponding to the simulations represented by Figs. 12 and 13 and the cases identified in Fig. 10 ($n = 151 \times 151 = 22\,801$). Shown are comparisons of cases 2, 3, and 4 with case 1, for hourly simulation data averaged over January and July. Highlighted is the degradation in model solution with a reduced number of meteorological stations in the domain.

	Case 2		Case 3		Case 4	
	r^2	Rmse	r^2	Rmse	r^2	Rmse
T_{air} (°C): Jan	0.96	0.2	0.91	0.4	0.87	0.6
T_{air} (°C): Jul	0.94	0.5	0.93	0.9	0.88	1.5
RH (%): Jan	0.93	1.6	0.85	2.8	0.84	4.1
RH (%): Jul	0.55	3.2	0.74	3.6	0.47	7.3

2) NORTH VERSUS SOUTH SLOPES

Consider a topographically variable domain with only one meteorological station. MicroMet will distribute the station temperature observation over that domain under an assumed lapse rate. A contour plot of the resulting temperature field will look like a topographic map of the area, but with units of temperature instead of elevation. In the natural system, we expect the temperature to vary as a function of slope and aspect, and their relationship to the incoming solar radiation. For example, in the Northern Hemisphere we expect that reduced solar radiation on north-facing slopes will have lower air temperatures, and south-facing slopes will experience greater temperatures. To compensate for this oversimplification, MicroMet could perform a surface energy budget calculation, under the assumption that the air temperatures above the two surfaces are initially the same (but incoming solar radiation levels are different), and the resulting combina-

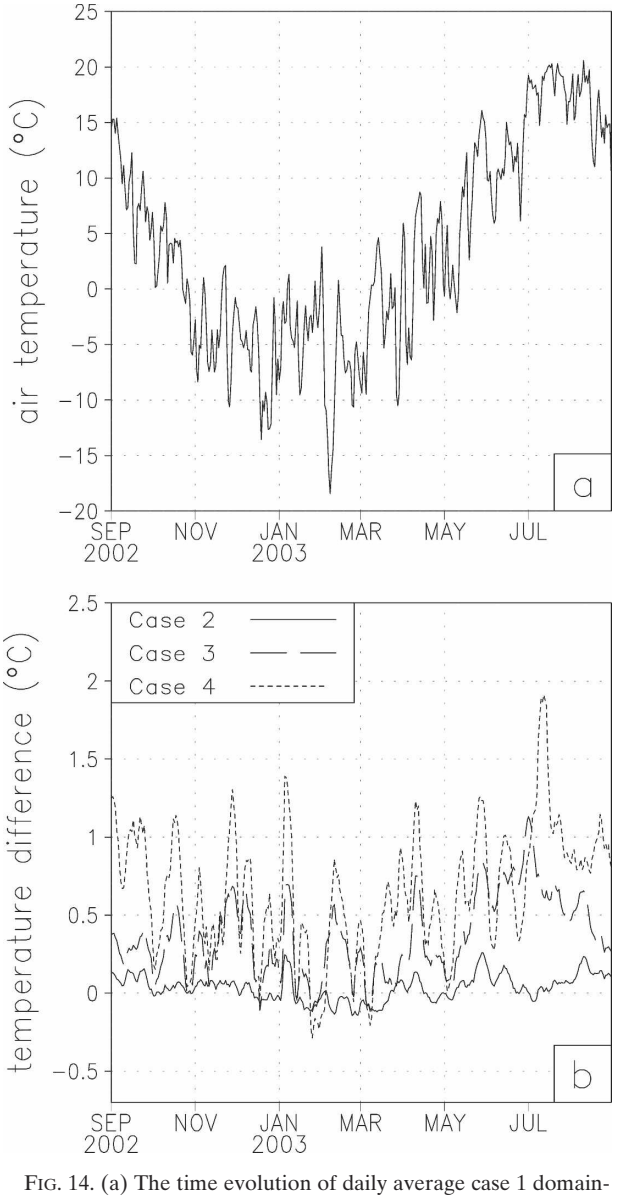

FIG. 14. (a) The time evolution of daily average case 1 domain-average air temperature. (b) Domain-average air temperature, case 2 minus case 1, case 3 minus case 1, etc.

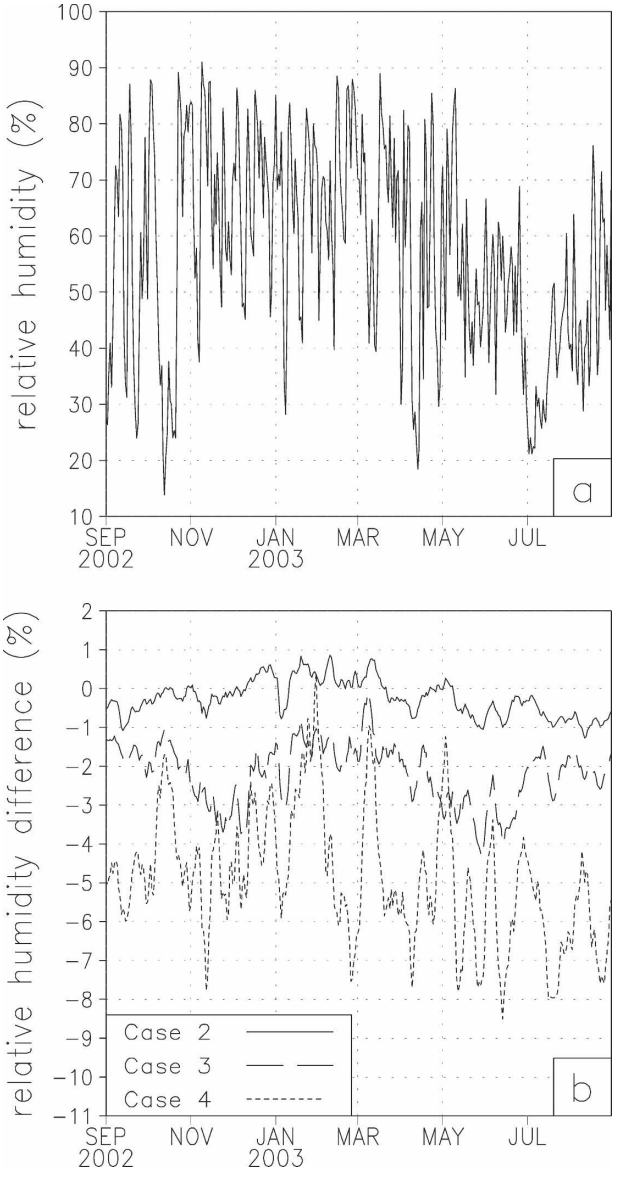

FIG. 15. (a) The time evolution of daily average case 1 domain-average relative humidity. (b) Domain-average relative humidity, case 2 minus case 1, case 3 minus case 1, etc.

tion of surface net radiation and sensible and latent heat fluxes could be used to modify initial air temperatures. This accounting also requires implementation of a coincident energy-balance/land surface hydrology model.

3) PRECIPITATION

Consider a simulation domain within the topographically complex western United States. With one meteorological tower, MicroMet will distribute the tower precipitation observation over the domain under an assumed precipitation adjustment factor (a precipitation lapse rate, of sorts). In contrast to the current model, the natural system includes significant orographically induced precipitation variability from western to eastern mountain slopes. MicroMet could resolve this by implementing a high-resolution orographic precipitation submodel (Hay and McCabe 1998; Pandey et al. 2000; Smith and Barstad 2004). In addition to orographic precipitation, other precipitation mechanisms and structures are not currently accounted for within MicroMet. For example, this version of MicroMet will not simulate the magnitudes and distributions of precipitation associated with convective storms that are

TABLE 4. Statistical information (square of the linear correlation coefficient, r^2, and rmse) corresponding to the simulations represented by Figs. 14 and 15, and the cases identified in Fig. 10 ($n = 365$). Shown are comparisons of cases 2, 3, and 4 with case 1, for daily averaged simulation data averaged over the Fig. 10 simulation domain. Highlighted is the degradation in model solution with a reduced number of meteorological stations in the domain.

	Case 2		Case 3		Case 4	
	r^2	Rmse	r^2	Rmse	r^2	Rmse
T_{air} (°C)	0.99	0.1	0.99	0.5	0.99	0.8
RH (%)	0.99	0.6	0.99	2.5	0.97	5.5

not captured by the station-observing network. It is clear that MicroMet's precipitation representation is its greatest weakness. Unfortunately, a viable solution (high resolution, computationally efficient, accurate, and valid for both large-scale, orographic, and convective precipitation systems) has not been found. As part of future MicroMet development efforts, improvements to its precipitation representation will be a top priority.

6. Conclusions

MicroMet interpolates irregularly distributed station observations to a regularly spaced grid using the Barnes objective analysis scheme. In addition to the station interpolations, MicroMet employs corrections based on known temperature–elevation, wind–topography, and solar radiation–topography relationships. The resulting procedures produce much-improved temperature, humidity, wind, and incoming solar and longwave radiation distributions when the spatial scale of topographic variability is smaller than the distance between stations or analyses-model grid points. In natural systems, this is nearly always the case.

The development of a model designed to take available, relatively coarse-resolution atmospheric datasets (e.g., meteorological station observations and/or atmospheric analyses) and convert them, in physically realistic ways, to high-resolution forcing data, is expected to lay the groundwork for substantial improvements to existing hydrologic and ecologic models. This need is particularly acute in regions where topographic variations lead to substantial variations in winter snow precipitation, snow-depth distribution, spring snowmelt, spring and summer runoff rates, evaporation, transpiration, and the wide range of associated energy and moisture fluxes.

Acknowledgments. The authors thank Christopher A. Hiemstra for his work and comments regarding an early version of this model, Angus Goodbody and Nick Rutter for their assistance with the meteorological station datasets, Daniel L. Birkenheuer for providing the LAPS data, and Christopher A. Hiemstra, Rudy King, Lixin Lu, Francisco Munoz, Laurie Porth, and three anonymous reviewers for their insightful comments on early versions of this paper. This work was supported by NASA Grants NAG5-11710, NNG04GP59G, and NNG04HK191, NOAA Grant NA17RJ1228, and National Science Foundation Grant 0229973.

REFERENCES

AMS, 1998: Weather analysis and forecasting: AMS Council Policy Statement adopted on 17 August 1998. *Bull. Amer. Meteor. Soc.,* **79,** 2161–2163.

Barnes, S. L., 1964: A technique for maximizing details in numerical weather map analysis. *J. Appl. Meteor.,* **3,** 396–409.

——, 1973: Mesoscale objective analysis using weighted time-series observations. NOAA Tech. Memo. ERL NSSL-62, National Severe Storms Laboratory, Norman, OK, 60 pp.

Box, G. E. P., and G. M. Jenkins, 1976: *Time Series Analysis, Forecasting, and Control.* Holden-Day, 575 pp.

Bruland, O., G. E. Liston, J. Vonk, and A. Killingtveit, 2004: Modelling the snow distribution at two high-Arctic sites at Svalbard, Norway, and at a sub-Arctic site in central Norway. *Nordic Hydrol.,* **35,** 191–208.

Buck, A. L., 1981: New equations for computing vapor pressure and enhancement factor. *J. Appl. Meteor.,* **20,** 1527–1532.

Burridge, D. M., and A. J. Gadd, 1974: The Meteorological Office operational 10 level numerical weather prediction model (December 1974). U.K. Met. Office Tech. Notes 12 and 48, 57 pp.

Burrough, P. A., and R. A. McDonnell, 2000: *Principles of Geographical Information Systems*. Oxford University Press, 333 pp.

Dodson, R., and D. Marks, 1997: Daily air temperature interpolation at high spatial resolution over a large mountainous region. *Climate Res.,* **8,** 1–20.

Greene, E. M., G. E. Liston, and R. A. Pielke Sr., 1999: Simulation of above treeline snowdrift formation using a numerical snow-transport model. *Cold Reg. Sci. Technol.,* **30,** 135–144.

Hasholt, B., G. E. Liston, and N. T. Knudsen, 2003: Snow distribution modelling in the Ammassalik region, South East Greenland. *Nordic Hydrol.,* **34** (1-2), 1–16.

Hay, L. E., and G. J. McCabe, 1998: Verification of the Rhea-orographic-precipitation model. *J. Amer. Water Res. Assoc.,* **34,** 103–112.

Hiemstra, C. A., G. E. Liston, and W. A. Reiners, 2002: Snow redistribution by wind and interactions with vegetation at upper treeline in the Medicine Bow Mountains, Wyoming, USA. *Arct. Antarct. Alp. Res.,* **34,** 262–273.

——, ——, and W. A. Reiners, 2006: Observing, modelling, and validating snow redistribution by wind in a Wyoming upper treeline landscape. *Ecol. Modell.,* in press.

Iziomon, M. G., H. Mayer, and A. Matzarakis, 2003: Downward atmospheric longwave irradiance under clear and cloudy skies: Measurement and parameterization. *J. Atmos. Sol.-Terr. Phys.,* **65,** 1107–1116.

Jasper, K., J. Gurtz, and H. Lang, 2002: Advanced flood forecasting in Alpine watersheds by coupling meteorological obser-

vations and forecasts with a distributed hydrological model. *J. Hydrol.,* **267,** 40–52.

Jolliffe, I. T., and D. B. Stephenson, 2003: *Forecast Verification: A Practitioner's Guide in Atmospheric Science.* John Wiley and Sons, 240 pp.

Koch, S. E., M. DesJardins, and P. J. Kocin, 1983: An interactive Barnes objective map analysis scheme for use with satellite and conventional data. *J. Climate Appl. Meteor.,* **22,** 1487–1503.

Kunkel, K. E., 1989: Simple procedures for extrapolation of humidity variables in the mountainous western United States. *J. Climate,* **2,** 656–669.

Kyle, H. L., P. E. Ardanuy, and E. J. Hurley, 1985: The status of the *Nimbus-7* Earth-Radiation-Budget data set. *Bull. Amer. Meteor. Soc.,* **66,** 1378–1388.

Le Dizès, S., B. L. Kwiatkowski, E. B. Rastetter, A. Hope, J. E. Hobbie, D. Stow, and S. Daescher, 2003: Modeling biogeochemical responses of tundra ecosystems to temporal and spatial variations in climate in the Kuparuk River Basin (Alaska). *J. Geophys. Res.,* **108,** 8165, doi:10.1029/2001JD000960.

Liston, G. E., 2004: Representing subgrid snow cover heterogeneities in regional and global models. *J. Climate,* **17,** 1381–1397.

——, and M. Sturm, 1998: A snow-transport model for complex terrain. *J. Glaciol.,* **44,** 498–516.

——, and R. A. Pielke Sr., 2001: A climate version of the regional atmospheric modeling system. *Theor. Appl. Climatol.,* **68,** 155–173.

——, and M. Sturm, 2002: Winter precipitation patterns in arctic Alaska determined from a blowing-snow model and snow-depth observations. *J. Hydrometeor.,* **3,** 646–659.

——, and J.-G. Winther, 2005: Antarctic surface and subsurface snow and ice melt fluxes. *J. Climate,* **18,** 1469–1481.

——, R. A. Pielke Sr., and E. M. Greene, 1999: Improving first-order snow-related deficiencies in a regional climate model. *J. Geophys. Res.,* **104** (D16), 19 559–19 567.

——, J.-G. Winther, O. Bruland, H. Elvehøy, K. Sand, and L. Karlöf, 2000: Snow and blue-ice distribution patterns on the coastal Antarctic ice sheet. *Antarct. Sci.,* **12,** 69–79.

——, J. P. McFadden, M. Sturm, and R. A. Pielke Sr., 2002: Modeled changes in arctic tundra snow, energy, and moisture fluxes due to increased shrubs. *Global Change Biol.,* **8,** 17–32.

Ludwig, R., and W. Mauser, 2000: Modeling catchment hydrology within a GIS based SVAT-model framework. *Hydrol. Earth Syst. Sci.,* **4,** 239–249.

Meek, D. W., and J. L. Hatfield, 1994: Data quality checking for single station meteorological variables. *Agric. For. Meteor.,* **69,** 85–109.

Mitchell, K. E., and Coauthors, 2004: The multi-institution North American Land Data Assimilation System (NLDAS): Utilizing multiple GCIP products and partners in a continental distributed hydrological modeling system. *J. Geophys. Res.,* **109,** D07S90, doi:10.1029/203JD003823.

Nash, J. E., and J. V. Sutcliffe, 1970: River flow forecasting through conceptual models. Part I—A discussion of principles. *J. Hydrol.,* **10,** 282–290.

Pandey, G. R., D. R. Cayan, M. D. Dettinger, and K. P. Georgakakos, 2000: A hybrid orographic plus statistical model for downscaling daily precipitation in northern California. *J. Hydrometeor.,* **1,** 491–506.

Pielke, R. A., Sr., 2001: Influence of the spatial distribution of vegetation and soils on the prediction of cumulus convective rainfall. *Rev. Geophys.,* **39,** 151–177.

Pohl, S., P. Marsh, and G. E. Liston, 2006: Spatial–temporal variability in turbulent fluxes during spring snowmelt. *Arct. Antarct. Alp. Res.,* **38,** in press.

Prasad, R., D. G. Tarboton, G. E. Liston, C. H. Luce, and M. S. Seyfried, 2001: Testing a blowing snow model against distributed snow measurements at Upper Sheep Creek, Idaho, USA. *Water Resour. Res.,* **37,** 1341–1357.

Randall, D., M. Khairoutdinov, A. Arakawa, and W. Grabowski, 2003: Breaking the cloud parameterization deadlock. *Bull. Amer. Meteor. Soc.,* **84,** 1547–1564.

Ryan, B. C., 1977: A mathematical model for diagnosis and prediction of surface winds in mountainous terrain. *J. Appl. Meteor.,* **16,** 571–584.

Shiklomanov, N. I., and F. E. Nelson, 2002: Active-layer mapping at regional scales: A 13-year spatial time series for the Kuparuk region, north-central Alaska. *Permafrost Periglac. Processes,* **13,** 219–230.

Smith, R. B., and I. Barstad, 2004: A linear theory of orographic precipitation. *J. Atmos. Sci.,* **61,** 1377–1391.

Taras, B., M. Sturm, and G. E. Liston, 2002: Snow–ground interface temperatures in the Kuparuk River basin, arctic Alaska: Measurements and model. *J. Hydrometeor.,* **3,** 377–394.

Thornton, P. E., S. W. Running, and M. A. White, 1997: Generating surfaces of daily meteorological variables over large regions of complex terrain. *J. Hydrol.,* **190,** 214–251.

Vourlitis, G. L., J. Verfaillie, W. C. Oechel, A. Hope, D. Stow, and R. Engstrom, 2003: Spatial variation in regional CO_2 exchange for the Kuparuk River basin, Alaska over the summer growing season. *Global Change Biol.,* **9,** 930–941.

Walcek, C. J., 1994: Cloud cover and its relationship to relative humidity during a spring midlatitude cyclone. *Mon. Wea. Rev.,* **122,** 1021–1035.

Wallace, J. M., and P. V. Hobbs, 1977: *Atmospheric Science: An Introductory Survey*. Academic Press, 467 pp.

Walton, T. L., Jr., 1996: Fill-in of missing data in univariate coastal data. *J. Appl. Stat.,* **23,** 31–39.

Westrick, K. J., P. Storck, and C. F. Mass, 2002: Description and evaluation of a hydrometeorological forecast system for mountainous watersheds. *Wea. Forecasting,* **17,** 250–262.

Whitaker, A., Y. Alila, J. Beckers, and D. Toews, 2003: Application of the Distributed Hydrological Soil Vegetation Model to Redfish Creek, British Columbia: Model evaluation using internal catchment data. *Hydrol. Processes,* **17,** 199–224.

Winstral, A., K. Elder, and R. E. Davis, 2002: Spatial snow modeling of wind-redistributed snow using terrain-based parameters. *J. Hydrometeor.,* **3,** 524–538.

Wood, E. F., D. P. Lettenmaier, X. Liang, B. Nijssen, and S. W. Wetze, 1997: Hydrological modeling of continental-scale basins. *Annu. Rev. Earth Planet. Sci.,* **25,** 279–300.